Microwave instability threshold from coherent wiggler radiation impedance in storage rings

A. Blednykh *
Brookhaven National Laboratory, Upton, New York 11973, USA

M. Blaskiewicz
Brookhaven National Laboratory, Upton, New York 11973, USA

R. Lindberg
Argonne National Laboratory, Argonne, Illinois 60439, USA

D. Zhou †
KEK, High Energy Accelerator Organization, Oho 1-1, Tsukuba 305-0801, Japan

(Received 28 February 2023; accepted 26 April 2023; published 17 May 2023)

The contribution of coherent wiggler radiation (CWR) to the microwave instability threshold in wiggler-dominated storage rings such as damping rings for colliders is discussed in detail. Three different coherent wiggler radiation impedance models are considered: the free-space steady-state model, the parallel-plates shielding steady-state model, and the rectangular-chamber shielding model. The field dynamics of CWR are compared, showing that the broad-band unshielded CWR becomes dominated by resonant structures when chamber shielding is considered. To suppress the narrow-band impedance in damping wigglers with chamber shielding, we propose employing a detuned damping wiggler. A new, simple, analytical method of solving the dispersion relation and detecting the CWR-driven microwave instability threshold is presented. The theory is compared with the numerical simulations of a Vlasov-Fokker-Planck solver for the Electron Ion Collider backup storage ring cooler and confirms that the microwave instability threshold gets higher for negative momentum compaction.

DOI: 10.1103/PhysRevAccelBeams.26.051002

I. INTRODUCTION

In storage rings, charged particle beams move along curved orbits inside dipole and wiggler magnets, which leads to the emission of coherent synchrotron radiation (CSR). CSR contributes to the beam coupling impedance and can be a source of the microwave instability. Compared to the impedance from discontinuities of vacuum chambers, the CSR impedance is typically more profound at high frequencies (corresponding to millimeter wave or shorter wavelengths) so that it often sets the numerical demands for simulations of the microwave instability. For the convenience of discussion, we use the terms CSR and coherent wiggler radiation (CWR) to indicate the coherent radiation from dipoles and wigglers, respectively.

Numerically predicting the instability thresholds due to CSR and CWR wakefields is a challenging task when studying collective effects in storage rings. Particle tracking codes often have difficulties in properly model high-frequency impedances due to CSR or CWR. As a first step, an analytical estimate of the instability threshold can be very helpful, especially during the initial stages when one is targeting the accelerator machine and beam parameters that will be below the instability threshold. In addition, the obtained instability threshold can be used as a reference value to help cross-check particle tracking simulations. Numerical simulations are necessary in any case since they give a global picture of the beam parameters below and above the instability threshold.

In recent years, there have been intensive investigations to calculate the CSR impedance (see, e.g., Refs. [1–6] and references therein) and compute the CSR-driven microwave instability (examples include Refs. [7–9] and references therein) for storage rings. Investigations have also been made into CWR impedance calculations (see, e.g., [6,10,11] and references therein). The CWR-driven

*Corresponding author.
blednykh@bnl.gov
†Corresponding author.
dmzhou@post.kek.jp

microwave instability using a steady-state CWR impedance model in free space was examined by Wu *et al.* in Ref. [12], which became the main reference in evaluating CWR effects in wiggler-dominated rings such as damping rings of colliders [13,14].

Recent developmental work on the backup ring cooler [15] for the Electron Ion Collider (EIC) [16] at Brookhaven National Laboratory (BNL) motivated us to revisit how CWR can affect the microwave instability. This is because the ring cooler concept employs a significant number of damping wigglers to reduce the equilibrium emittance. One of the main concerns in achieving the required beam parameters is related to collective effects, particularly, the effect of coherent synchrotron radiation produced by the damping wigglers (DWs). We believe that contribution of CWR to the total impedance budget is significant, especially for ∼16 DWs at low-energy ring.

This paper is organized as follows: In Sec. II, we revisit the analytic theories developed in Ref. [6] for CWR impedance and derive a simple formula for the steady-state CWR impedance with parallel-plates shielding. Meanwhile, we document the existing analytical models of the low-frequency steady-state CWR impedance, the steady-state CWR impedance for parallel-plates shielding, and the CWR impedance for a damping wiggler with rectangular vacuum chamber. These analytic approaches are compared with numerical calculations from the CSRZ code [5,17] using the EIC backup ring cooler parameters as an example. In Sec. III, we present an idea of designing detuned wigglers to suppress the narrow-band CWR impedance. In Sec. IV, we apply the instability analysis of Ref. [7] to derive a simple scaling law of CWR instability. Numerical simulations of microwave instability with three models of CWR impedance are presented in Sec. V B. Finally, we summarize our findings in Sec. VI.

II. IMPEDANCE MODELS FOR DAMPING WIGGLERS WITH A CONSTANT PERIOD

We start from the formulations of Ref. [6] to derive the analytic models for CWR impedance. The beam orbit inside a plane wiggler with periodic fields can be described by

$$x(z) = -\frac{\theta_0}{k_w}\cos(k_w z), \tag{1}$$

where $k_w = 2\pi/\lambda_w$ with λ_w, the wiggler's period length, and $\theta_0 = K/\gamma$ is the deflection angle defined in terms of the dimensionless wiggler strength $K \approx 93.4 B_w \lambda_w$ (B_w is the peak wiggler magnetic field in Tesla while λ_w is in meters) and the Lorentz factor γ. We will be concerned with frequencies below the critical photon frequency so we assume the electrons travel at the speed of light. The horizontal and longitudinal relative velocities of the beam are

$$\beta_x = \theta_0 \sin(k_w z), \tag{2}$$

$$\beta_z = 1 - \frac{1}{2}\theta_0^2 \sin^2(k_w z). \tag{3}$$

The wiggling motion slows down the average velocity in z direction. Consequently, the arc length s measured along the beam orbit is approximated by

$$s(z) \approx z\left(1 + \frac{1}{4}\theta_0^2\right) - \frac{\theta_0^2}{8k_w}\sin(2k_w z). \tag{4}$$

A. Free-space steady-state model

The low-frequency steady-state CWR impedance in free space can be calculated from Eq. (D7) of Ref. [6] as

$$\frac{Z_L(k)}{L} \approx \frac{iZ_0\theta_0^2 k}{4\pi}\int_0^\infty d\nu \frac{1}{\nu}\sin^2\frac{\nu}{2} e^{-\frac{1}{4}ir\nu}, \tag{5}$$

with $r = k\theta_0^2/k_w$. The integral over ν can be done analytically, with its real part surprisingly independent of r but its imaginary part dependent on r, yielding

$$\frac{Z_L(k)}{L} \approx \frac{1}{16} Z_0\theta_0^2 k\left[1 - \frac{2i}{\pi}\ln\left(\frac{\theta_0^2 k}{4k_w}\right)\right]. \tag{6}$$

This is the low-frequency limit of the steady-state CWR impedance model in free space [6,10], which is valid provided $r \ll 1$, $\theta_0 \ll 1$, and $K \gg 1$. The real part of the CWR impedance indicates the amplitude of the radiation power spectrum, which is proportional to θ_0^2. The imaginary part of the CWR impedance contains a space-charge-like term which is related to the slowdown of the beam in z direction due to wiggling motion [see Eq. (4)]. This feature is similar to CSR, which contains overtaking fields, causing energy gain for the head part of a bunch.

B. Parallel-plates shielding steady-state model

The steady-state CWR impedance with parallel-plate shielding is formulated using Eq. (D4) of Ref. [6]. But here we seek a simpler formula that applies in the limit of low frequencies $r \ll 1$. We start from Eq. (D7) of Ref. [6] but recover the summation over waveguide modes

$$\frac{Z_L(k)}{L} \approx \frac{(i-1)Z_0\theta_0^2\sqrt{\pi k}}{2\pi b\sqrt{k_w}}\sum_{n=0}^{\infty}\int_0^\infty d\nu \times \frac{1}{\sqrt{\nu}}\sin^2\frac{\nu}{2} e^{-\frac{1}{4}ir\nu} e^{-i\nu\frac{(2n+1)^2\pi^2}{2kk_w b^2}}, \tag{7}$$

where b is the full gap between two parallel plates. The exponent term containing n results from an expansion of the square root term of the longitudinal wave number (see Eq. (24) of Ref. [6]). Here we also recover it tentatively for later discussions of the field dynamics of CWR

$$\frac{Z_L(k)}{L} \approx \frac{(i-1)Z_0\theta_0^2\sqrt{\pi k}}{2\pi b\sqrt{k_w}} \sum_{n=0}^{\infty} \int_0^{\infty} d\nu \times \frac{1}{\sqrt{\nu}} \sin^2\frac{\nu}{2} e^{-\frac{1}{4}ir\nu} e^{-\frac{i\nu}{k_w}(k-\sqrt{k^2-k_n^2})}, \quad (8)$$

with $k_n = \frac{(2n+1)\pi}{b}$. Replacing ν by $\xi = \nu/(kk_w b^2)$, we obtain

$$\frac{Z_L(k)}{L} \approx \frac{(i-1)Z_0\theta_0^2 k}{2\sqrt{\pi}} \sum_{n=0}^{\infty} F_n(k), \quad (9)$$

with

$$F_n(k) = \int_0^{\infty} d\xi \frac{1}{\sqrt{\xi}} \sin^2(D\xi) e^{-iB\xi}, \quad (10)$$

where we define $D = \frac{kk_w b^2}{2}$ and $B = \frac{1}{4}rkk_w b^2 + kb^2(k - \sqrt{k^2 - k_n^2})$. The integral over ξ can be done analytically (For instance, one can use *Mathematica* with the condition of $2D > B > 0$):

$$F_n(k) = \frac{1}{8B\sqrt{4D^2 - B^2}} \Big[-2\sqrt{\pi}B\sqrt{2D + \sqrt{4D^2 - B^2}} + i\sqrt{2\pi}B(\sqrt{2D - B} - \sqrt{2D + B}) + (2-2i)\sqrt{2\pi}\sqrt{4D^2B - B^3} \Big]. \quad (11)$$

One can see that $F_n(k)$ has a singularity at

$$2D = B, \quad (12)$$

which indicates the resonant condition resulting from synchronicity between the waveguide modes and the beam motion [6]. The above resonant condition can be rewritten as

$$k = \bar{\beta}_z(k_z + k_w) \quad (13)$$

with $\bar{\beta}_z = 1/(1 + \frac{1}{4}\theta_0^2)$, the average longitudinal relative velocity and $k_z = \sqrt{k^2 - k_n^2}$, the longitudinal wave number in the presence of parallel-plates shielding. This resonant condition is a special case of a more generic one which was formulated in Ref. [17] [Eq. (3.116) therein]. Equation (13) can also be interpreted as the dispersion relation as shown in Fig. 1. There are several observations deserving clarification here: (i) The dashed black lines $k = \pm k_z$ indicate the case of beam motion with $\bar{\beta}_z = 1$ (i.e., the ultrarelativistic case); (ii) The solid red lines indicate the dispersion relation of waveguide modes with their phase velocity $v_p \equiv ck/k_z$ larger than c, but group velocity $v_g \equiv cdk/dk_z$ (i.e., speed of energy transfer) smaller than c; (iii) The solid blue lines indicate the harmonics of beam's wiggling motion. The slope of the beam mode is determined by $\bar{\beta}_z < 1$. The beam motion

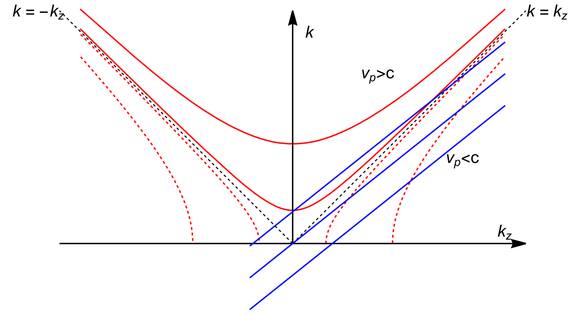

FIG. 1. Dispersion relation for the waves propagating along a waveguide sandwiched by a wiggler. The solid blue lines from top to bottom indicate the beam modes of $k = \bar{\beta}_z(k_z + k_w)$, $k = \bar{\beta}_z k_z$, and $k = \bar{\beta}_z(k_z - k_w)$.

is modulated by wiggler fields by pk_w with p indicating the pth harmonic of wiggling motion. The dominant term for wiggler radiation is from $p = 1$.

With chamber shielding, the solutions of Eq. (13) define the resonant frequencies, which can be found by solving a quadratic equation of k as follows

$$k_{r\pm} = \frac{\bar{\beta}_z}{1 - \bar{\beta}_z^2} \left[k_w \pm \sqrt{\bar{\beta}_z^2 k_w^2 - (1 - \bar{\beta}_z^2)k_n^2} \right]. \quad (14)$$

Expanding the square root and only keeping the leading term, we can find the approximate expressions of the above equation as

$$k_{r+} \approx \frac{4k_w}{\theta_0^2} - \frac{k_n^2}{2k_w}, \quad (15)$$

and

$$k_{r-} \approx \frac{\bar{\beta}_z k_w}{1 + \bar{\beta}_z} + \frac{k_n^2}{2k_w}. \quad (16)$$

Here k_{r+} and k_{r-} correspond to the $+$ and $-$ signs inside the square brackets of Eq. (14), respectively. They represent the resonant frequencies of CWR at the high- and low-frequency limits, respectively.

The physical meanings of k_{r+} and k_{r-} can be seen more clearly when we consider two extreme cases: $\theta_0 \to 0$ and $b \to \infty$.

For the limit of $\theta_0 \to 0$ ($\theta_0 \ll 1$ is usually true for damping wigglers), Eq. (13) can be approximated by

$$k - k_w \approx k_z, \quad (17)$$

with $\bar{\beta}_z \approx 1$. Then, the resonant frequencies have a simple form of

$$k_r = \frac{1}{2}k_w + \frac{k_n^2}{2k_w}, \tag{18}$$

which corresponds to Eq. (16) with $\bar{\beta}_z = 1$. When $\theta_0 \to 0$, $k_{r+} \to \infty$ is of no interest.

For the limit of $b \to \infty$ (i.e., without chamber shielding), there is $k_n = 0$. The resonant frequencies from Eq. (13) are determined by

$$k_c = \frac{4k_w}{\theta_0^2}, \tag{19}$$

which corresponds to Eq. (15) with $k_n = 0$. Note that k_c is exactly the fundamental radiation frequency of a wiggler. This frequency is determined by the crossing point of $k = \bar{\beta}_z(k_z + k_w)$ and $k = k_z$ (as shown in Fig. 1) and is usually very large with $\theta_0 \ll 1$ and $k_w \gg 1\ \mathrm{m}^{-1}$.

The previous analysis shows that Eq. (8) contains the essential field dynamics of CWR and is suitable for calculating the CWR impedance of damping wigglers. As an example, the steady-state CWR impedance models in free space [Eq. (6)] and parallel plates [Eq. (9)] are tested using the case of the EIC ring cooler with its wiggler parameters shown in Table I. The results of impedances and wakefields for a 0.3-mm Gaussian bunch length are compared in Figs. 2 and 3. The chosen maximum wave number for the impedance data is $k_{\max} = 20\,000\ \mathrm{m}^{-1}$, which is high enough for the 0.3-mm Gaussian bunch's wakefield. Also, note that $k_{\max} \ll k_c \approx 6.2 \times 10^5\ \mathrm{m}^{-1}$ for the case of the EIC backup ring cooler, suggesting that we are only looking at the low-frequency CWR impedance. One can see that the narrow spikes in the CWR impedance due to parallel-plates shielding create the oscillatory long-range wakefield trailing behind the bunch (narrow-band impedance). On the other hand, the parallel plates shield the low-frequency waves, reducing the amplitude of short-range wakefields.

To check that Eq. (9) with Eq. (11) correctly describes the CWR impedance with parallel-plates shielding, we try another example by enlarging the full chamber height from 15 to 60 mm. The results are shown in Figs. 4 and 5. As expected, the impedance and short-range wakefield approach the free-space model when the chamber is opened.

TABLE I. Preliminary damping wiggler parameters for the EIC backup ring cooler.

Magnetic field, B	T	1.9
Length, L	m	7.44
Bending radius, ρ	m	0.246
Wiggler period, λ_w	mm	48
Number of poles, N_p		155
Vertical full chamber height, b	mm	15
Horizontal full chamber width, a	mm	45
Number of DWs, N_w		16

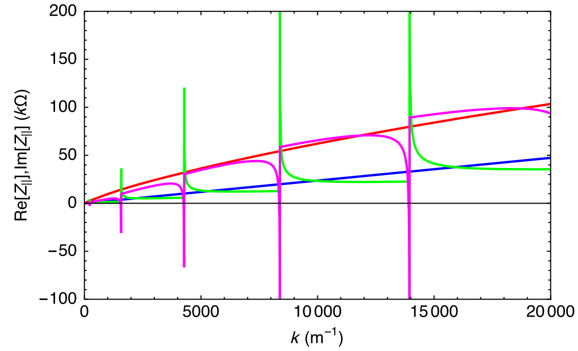

FIG. 2. Comparison of CWR impedance in free space and parallel-plates shielding (full chamber height is 15 mm) for the 16 DWs of the backup storage ring cooler. Blue and red lines are real and imaginary parts of CWR impedance in free space. Green and magenta lines are real and imaginary parts of CWR impedance in parallel-plates shielding (Note that the amplitudes of resonance peaks should go to $\pm\infty$ according to Eq. (11). Because of off-resonance sampling, the plot shows finite amplitudes).

C. Rectangular-chamber shielding model

The DW vacuum chambers usually have a closed cross section instead of parallel plates, in which case, a rectangular chamber serves as better approximation for the chamber's geometry. The relevant theories of CWR impedance have been investigated in Refs. [11,17,18]. The CSRZ code was originally developed to calculate CSR impedance, but it can also calculate the CWR impedance for a rectangular chamber in the limit that the wiggle motion is much smaller than the chamber dimensions [17]. In this subsection, we compare the theories and CSRZ calculations to reveal the field dynamics of CWR.

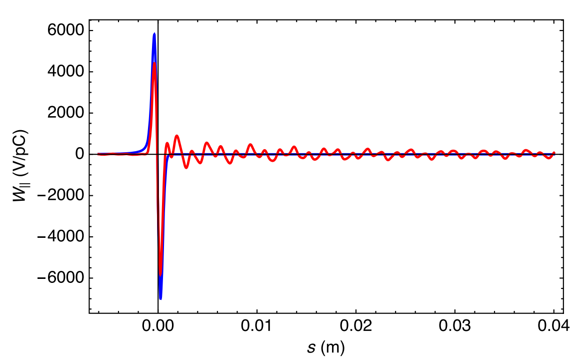

FIG. 3. Comparison of CWR wakefield of a 0.3-mm Gaussian bunch in free space and parallel-plates shielding (full chamber height is 15 mm) for the 16 DWs of backup storage ring cooler. Blue and red lines are for free space and parallel-plates shielding, respectively.

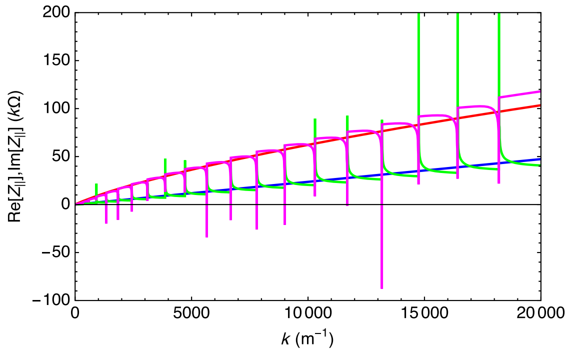

FIG. 4. Comparison of CWR impedance in free space and parallel-plates shielding for the 16 DWs of storage ring cooler. The full chamber height is 60 mm. Blue and red lines are real and imaginary parts of CWR impedance in free space. Green and magenta lines are real and imaginary parts of CWR impedance in parallel-plates shielding (Note that the amplitudes of resonant peaks should go to $\pm\infty$ according to Eq. (11). Because of off-resonance sampling, the plot shows finite amplitudes).

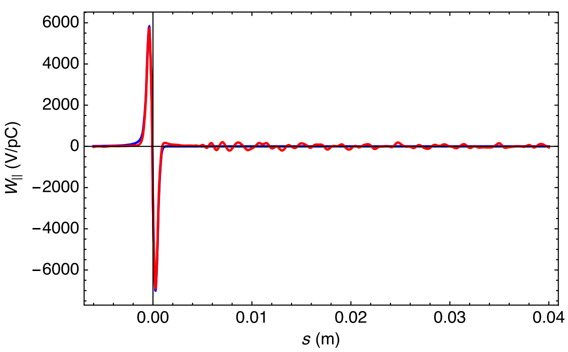

FIG. 5. Comparison of CWR wakefield of a 0.3-mm Gaussian bunch in free space and parallel-plates shielding for the 16 DWs of the backup storage ring cooler. The full chamber height is 60 mm. Blue and red lines are for free space and parallel-plates shielding, respectively.

1. Analytical approach

For the case of the rectangular-chamber shielding model, Stupakov and Zhou [11] have presented an analytical approach using the mode expansion method and obtained the real part of the CWR impedance

$$\mathrm{Re}Z_\parallel(k) = 4Z_0\theta_0^2 F(k), \tag{20}$$

where

$$F(k) = \frac{k_w^2}{abk}\sum_{m,n}\frac{1}{k_z}\left[\frac{k^2k_y^2}{\varkappa^2(1+\delta_{0,m})} + k_x^2\left(\frac{k_z}{\varkappa} - \frac{\varkappa}{k-k_z}\right)^2\right] \times \frac{\sin^2[\pi N_p(k-k_z)/k_w]}{[(k-k_z)^2-k_w^2]^2}, \tag{21}$$

with the horizontal, vertical, and longitudinal wave numbers, respectively, defined by $k_x = \frac{\pi m}{a}$, $k_y = \frac{\pi n}{b}$, $k_z = \sqrt{k^2-\varkappa^2}$ where $\varkappa = \sqrt{k_x^2+k_y^2}$, and δ is the Kronecker delta. The function $F(k)$ can be simplified to

$$F(k) = \frac{k_w^2}{abk}\sum_{m,n}\frac{\sin^2[\pi N_p(k-k_z)/k_w]}{[(k-k_z)^2-k_w^2]^2} \times \frac{1}{k_z}\left[\frac{k^2k_y^2}{\varkappa^2(1+\delta_{0,m})} + \frac{k_x^2k^2}{\varkappa^2}\right]. \tag{22}$$

Equation (20) with Eq. (21) was obtained with the beam orbit defined by

$$x(z) = \frac{\theta_0}{k_w}[1-\cos(k_w z)], \tag{23}$$

and further assumption of $\bar{\beta}_z = 1$. The reader may notice that Eq. (23) is slightly different from Eq. (1) with a constant offset. This offset impacts the final formula for $F(k)$ but does not change the key physics of the resonant structure in CWR impedance. The reader is also reminded that the mode expansion method was first used to calculate the coherent undulator impedance in Ref. [18]. It was also recognized that this method has a challenge in obtaining a converged formulation for the imaginary part of CWR impedance [17].

Equation (21) approximates the wiggler radiation impedance using the first harmonic of the beam motion, where the waveguide modes are in synchronism with the beam motion so that only the waveguide modes with even m and odd n can be synchronized with the $p=1$ harmonic. Therefore, the summation in Eq. (21) is for $m = 0, 2, 4, 6, \ldots$, and $n = 1, 3, 5, 7, \ldots$. The synchronization function in Eq. (21) is essential in defining the feature of the impedance spectrum. When the number of periods N_p is large, the impedance spectrum is highly peaked at k satisfying

$$k - k_z = k_w. \tag{24}$$

As detailed in Ref. [17], the general resonance condition is

$$k - k_z = pk_w, \tag{25}$$

with the index p indicating the harmonic number of beam oscillation when traversing the wiggler. The resonance frequencies are found at

$$k_{m,n} = \frac{p^2k_w^2+\varkappa^2}{2pk_w}. \tag{26}$$

Usually, the terms with $p=1$, which correspond to Eq. (20), dominate the impedance spectrum.

2. Numerical calculation using the CSRZ code

The CSRZ code [5,17] solves the parabolic equation with curvilinear coordinates in the frequency domain

$$\frac{\partial \vec{E}_\perp}{\partial s} = \frac{i}{2k}\left[\nabla_\perp^2 \vec{E}_\perp - \frac{1}{\epsilon_0}\nabla_\perp \rho_0 + \frac{2k^2 x}{\rho(s)}\vec{E}_\perp\right], \tag{27}$$

where $\vec{E}_\perp = (E_x, E_y) = (\mathcal{E}_x, \mathcal{E}_y)e^{-iks}$ is the slow-varying amplitude of the transverse electric field $(\mathcal{E}_x, \mathcal{E}_y)$ (see Refs. [17,19] for detailed formulations.), $k = \omega/c$ is the wave number, $\rho(s)$ is the s-dependent bending radius along the beam orbit, and ρ_0 is the charge density. Here we take the ultrarelativistic limit $\gamma \to \infty$, and $\nabla_\perp^2$ indicates the transverse Laplacian. Within the paraxial approximation, the slow-varying amplitude of the longitudinal field is calculated from the transverse field by

$$E_s = \frac{i}{k}(\nabla_\perp \cdot \vec{E}_\perp - \mu_0 c J_s), \tag{28}$$

where the current density $J_s = \rho_0 c$.

Here we illustrate how the paraxial approximation impacts predictions for the CWR problem. Using Maxwell's equation in Cartesian coordinates, in the ultrarelativistic limit, the exact equation for the slow-varying amplitude of the electric field is [17]

$$\frac{\partial \vec{E}_\perp}{\partial s} = \frac{i}{2k}\left[\nabla^2 \vec{E}_\perp - \frac{1}{\epsilon_0}\nabla_\perp \rho_0\right]. \tag{29}$$

Applying the paraxial approximation conditions of

$$\left|\frac{\partial^2 E_u}{\partial s^2}\right| \ll \left|k\frac{\partial E_u}{\partial s}\right| \ll |k^2 E_u|, \quad \text{with} \quad u = x \,\text{or}\, y, \tag{30}$$

the wave equation [Eq. (29)] reduces to

$$\frac{\partial \vec{E}_\perp}{\partial s} = \frac{i}{2k}\left[\nabla_\perp^2 \vec{E}_\perp - \frac{1}{\epsilon_0}\nabla_\perp \rho_0\right]. \tag{31}$$

Using E_x as an example, applying the mode expansion method to the full-wave equation [Eq. (29)] yields the solution

$$E_x = E_{x0}\,\sin(k_x x)\,\cos(k_y y)e^{-i(k-k_z)s}. \tag{32}$$

On the other hand, the analogous mode expansion solution of the paraxial Eq. (31) is

$$E_x = E_{x0}\,\sin(k_x x)\,\cos(k_y y)e^{-i\frac{k_x^2+k_y^2}{2k}s}. \tag{33}$$

It is trivial to derive the approximate Eq. (33) from Eq. (32) if we assume that

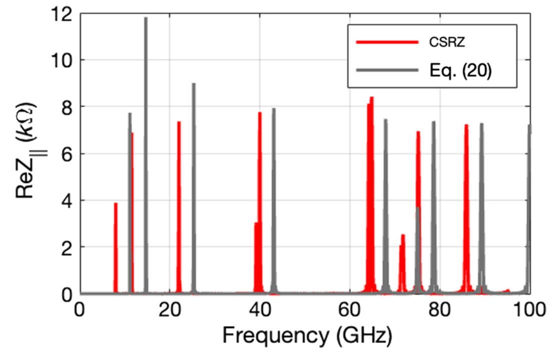

FIG. 6. Real part of the longitudinal impedance for one DW with the constant period length.

$$k - k_z \approx \frac{k_x^2 + k_y^2}{2k} = \frac{\varkappa^2}{2k}. \tag{34}$$

This approximation is equivalent to (30) for the case of CWR in a rectangular waveguide. In the context of this paper, we will use it to discuss resonant conditions that depend on the beam motion's synchronism with the waveguide modes. Equation (34) can be generalized into

$$\sqrt{k^2 - k_\perp^2} \approx k - \frac{k_\perp^2}{2k}, \tag{35}$$

with $k_\perp$ indicating the transverse wave number defined by transverse boundary conditions from the chamber. This is the paraxial approximation for fields propagating inside a waveguide with a general cross section.

3. Comparison of analytical and numerical calculations

The real and imaginary parts of the CWR impedance for a constant period damping wiggler are plotted in Figs. 6 and 7. Here, we use the nominal parameters of a potential EIC ring cooler that has $B_w = 1.9$ T, $\lambda_w = 0.048$ m, $N_p = 158$, $b = 15$ mm, and $a = 45$ mm, where b and a are the full vertical and horizontal apertures of the

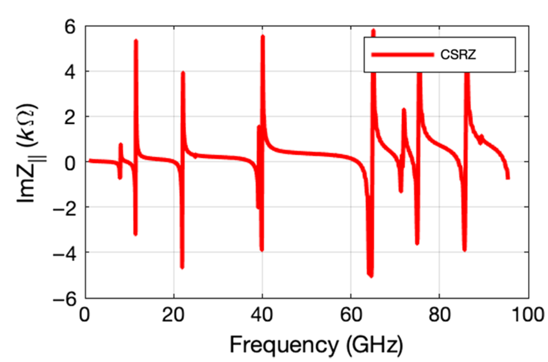

FIG. 7. Imaginary part of the longitudinal impedance for one DW with the constant period length.

rectangular vacuum chamber (Table I). The red traces are the numerically simulated data by the CSRZ code, whereas the gray trace is the result of the real part of the longitudinal impedance from Eq. (20). As can be seen, the spikes predicted by the two methods are shifted relative to each other by 3.1 GHz. The difference can be explained as follows: the CSRZ code solves the parabolic equation instead of the full Maxwell's equations. For the problem of wiggler radiation, the paraxial approximation implies taking the approximation of Eq. (34), in which case, the resonant frequencies predicted by CSRZ will be

$$k_{m,n}^{\mathrm{CSRZ}} = \frac{\varkappa^2}{2pk_w}. \tag{36}$$

Comparing Eq. (36) with Eq. (26), one can see that for $p = 1$, the peak positions will be shifted by an amount of $k_w/2$, which corresponds to $\Delta f \approx 3.1$ GHz for the DW parameters of the ring cooler shown in Fig. 6.

We also can identify and classify the narrow-band high-Q peaks predicted by both simulations and the analytical approach. They all correspond to H mode as illustrated in Fig. 8. The lowest-order mode in a rectangular vacuum chamber with $H_z \neq 0$ and $E_z = 0$, and $m = 0, 2, 4, 6, \ldots$, and $n = 1, 3, 5, 7, \ldots$, can be classified as H_{01} mode at frequency $f_1 = 11.1$ GHz with $a = 45$ mm and $b = 15$ mm. Hence, the next generated modes are H_{21} mode, H_{41} mode, and H_{61} mode at frequencies $f_2 = 14.6$ GHz, $f_3 = 25.3$ GHz, and $f_4 = 43.1$ GHz, respectively. The electric and magnetic field patterns of the first two modes, H_{01} mode and H_{21} mode, are shown in Fig. 8.

Figure 9 compares CWR wake potentials for three CWR models: free space steady state (blue line), rectangular chamber simulated by CSRZ (red line), and two parallel plates (green line). It is seen that the rectangular chamber shielding introduces more resonant peaks in the impedance and oscillatory long tail in the wake potential. The discrepancy in the short-range wake potentials between CSRZ and the parallel plates model might come from the paraxial approximation used in CSRZ calculation. This needs to be further investigated.

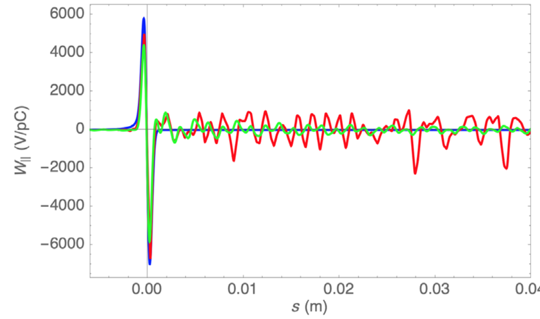

FIG. 9. Comparison of CWR wake potentials for the backup ring cooler with 0.3 mm Gaussian bunch. Blue line: free space model; red line: CSRZ model; green line: parallel plates model.

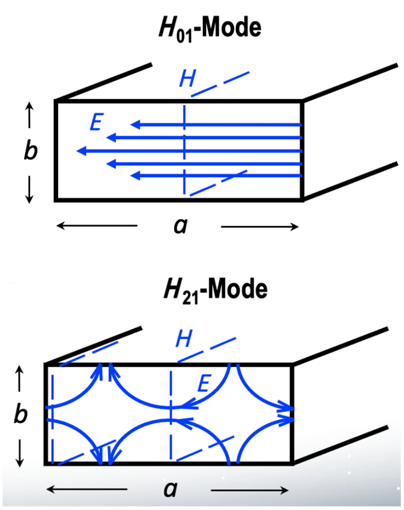

FIG. 8. Electric and magnetic fields pattern of H_{01} mode and H_{21} mode in a rectangular waveguide.

III. DAMPING WIGGLERS WITH A VARIED PERIOD LENGTH

In this section, we discuss one way to suppress the narrow-band impedance peaks observed and discussed in the previous section. The main idea is to spread the resonance frequency of each mode so that a high-Q peak becomes broader and smaller in magnitude. This general technique was first developed and applied for HOM suppression in the multi-cell accelerator structures [20], where each neighboring cavity differs in dimensions (radius and length) from the previous one. The spread in resonance frequencies can be achieved in a DW by, e.g., varying the wiggler period length. This technique is more convenient for a DW than for an accelerating structure since we need not to concern ourselves with maintaining the fundamental mode. In the numerical simulations, the DW period length is varied as $\lambda_i = \lambda_w + (i-1)\Delta\lambda$, where $i = 1, 2, 3, \ldots, N_p$. The number of periods is $N_p = 141$ and the difference between the following periods is $\Delta\lambda = 70$ μm. These parameters were chosen to keep the total length close to the length of the DW with a constant period. The difference in length between the last and the first period is within ~20%, and it is changed from $\lambda_1 =$ 48 mm to $\lambda_{141} = 58$ mm. The real and imaginary parts of the longitudinal impedance for a DW with varied (blue trace) and constant period (red trace) are presented in Figs. 10 and 11. The narrow-band impedance has been significantly suppressed due to the spread in resonant frequencies. However, the detuned DW does not affect the short-range wakefield, which is shown in Fig. 12, for a 0.3-mm bunch length.

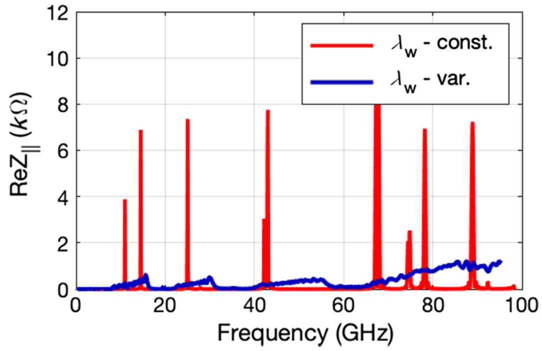

FIG. 10. Real part of the longitudinal impedance for one DW with constant and varied period lengths.

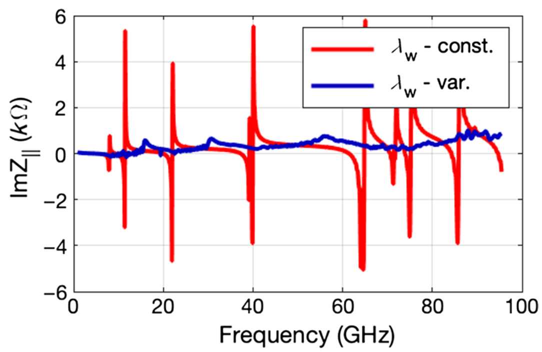

FIG. 11. Imaginary part of the longitudinal impedance for one DW with constant and varied period lengths.

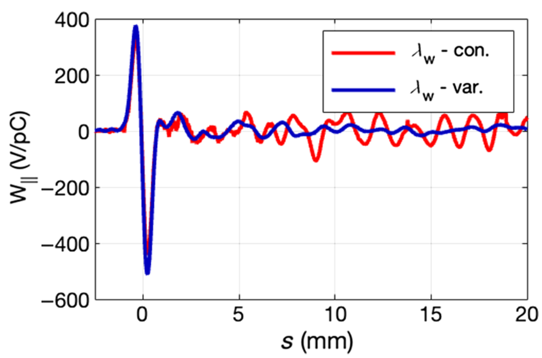

FIG. 12. Comparison of CWR wakefields for the DW with constant and varied period lengths for a 0.3 mm Gaussian bunch length.

IV. INSTABILITY ANALYSIS

For high-frequency impedances with $k\sigma_z \gg 1$, which is usually the case for CSR and CWR, the microwave instability (MWI) threshold can be determined by solving the dispersion relation for a coasting beam [7]

$$-if(I_b)\frac{Z_{\parallel}(k)}{k}G(A) = 1, \tag{37}$$

with

$$f(I_b) = \frac{I_b}{2\pi(E/e)\eta\sigma_p^2\sigma_z}, \tag{38}$$

and

$$G(A) = \int_{-\infty}^{\infty} dp \frac{pe^{-p^2/2}}{A+p}, \tag{39}$$

where $A = \Omega/(ck\eta\sigma_p)$ with $\eta = \alpha_c - \frac{1}{\gamma^2}$ the slip factor and α_c the momentum compaction. We simply take $\eta \approx \alpha_c$ in this paper with very large γ assumed. The beam is unstable if $\mathrm{Im}[\Omega] > 0$ with Im[] indicating the operation of taking the imaginary part. The dispersion relation Eq. (37) can be rewritten as

$$\frac{Z_{\parallel}(k)}{k} = \frac{i}{f(I_b)G(A)}, \tag{40}$$

with the left side representing the impedance normalized by frequency and the right side containing machine parameters.

There are alternative ways of solving Eq. (40) with given $Z_{\parallel}(k)/k$. Here we present a simple method that utilizes the explicit solution of Eq. (39) [21]. Assume $\mathrm{Im}[A] \neq 0$, the explicit form of $G(A)$ is

$$G(A) = \sqrt{2\pi} + i\pi A e^{-\frac{A^2}{2}}\left\{\mathrm{sgn}\{\mathrm{Im}[A]\} + i\,\mathrm{erfi}\left[\frac{A}{\sqrt{2}}\right]\right\}, \tag{41}$$

where $\mathrm{erfi}[z] = -i\frac{2}{\sqrt{\pi}}\int_0^{iz} e^{-t^2}dt$ is the imaginary error function and $\mathrm{sgn}[z]$ indicates the sign function. Note that Eq. (40) with Eq. (41) is valid for both positive and negative slip factors. Furthermore, solutions of Eq. (41) satisfy $\Omega(k) = -\Omega(-k)^*$ [7] as can be seen by taking the complex conjugate and using $Z_{\parallel}(k)^* = Z_{\parallel}(-k)$ and $G(A)^* = G(A^*)$. Hence, we need only consider positive k in what follows.

The criteria for detecting the instability is $\mathrm{Im}[\Omega] > 0$. Then solving Eq. (40) with $\mathrm{Im}[\Omega] = 0$ defines a boundary in the complex impedance plane to detect the instability threshold [22]. With $\mathrm{Im}[\Omega] = 0$, $A = A_r$ becomes real with its sign depending on the sign of η. For the convenience of calculation, we rewrite $Z_{\parallel}(k)$ and $G(A_r)$ in terms of their real and imaginary parts as follows:

$$\frac{Z_{\parallel}(k)}{k} = Z_r(k) + iZ_i(k), \tag{42}$$

$$G(A_r) = G_r(A_r) + iG_i(A_r). \tag{43}$$

With real values of k and A_r, we have

$$G_r(A_r) = \sqrt{2\pi} - \pi A_r e^{-A_r^2/2}\mathrm{erfi}[A_r/\sqrt{2}], \tag{44}$$

$$G_i(A_r) = \mathrm{sgn}[\eta]\pi A_r e^{-A_r^2/2}. \tag{45}$$

Applying the above variables to the dispersion relation Eq. (40) yields

$$\frac{G_i(A_r)}{G_r(A_r)} = \frac{Z_r(k)}{Z_i(k)}, \tag{46}$$

$$f_{\mathrm{th}}(G_r Z_i + G_i Z_r) = 1. \tag{47}$$

From the above equations, the threshold bunch current can be determined as

$$f_{\mathrm{th}} = \frac{Z_r}{G_i(Z_r^2 + Z_i^2)} = \frac{Z_i}{G_r(Z_r^2 + Z_i^2)}. \tag{48}$$

One can see that the threshold bunch current depends on the sign of the slippage factor and the aspect ratio of the real and imaginary parts of the impedance. In practical calculations, given impedance data at specified k, Eq. (46) is used to evaluate A_r, and then Eq. (48) is used to find the threshold current. For positive η, the properties of functions $G_r(A_r)$ and $G_i(A_r)$ with real A_r are shown in Fig. 13.

In the following, we test our method with two cases: Free-space steady-state CSR and CWR impedance models.

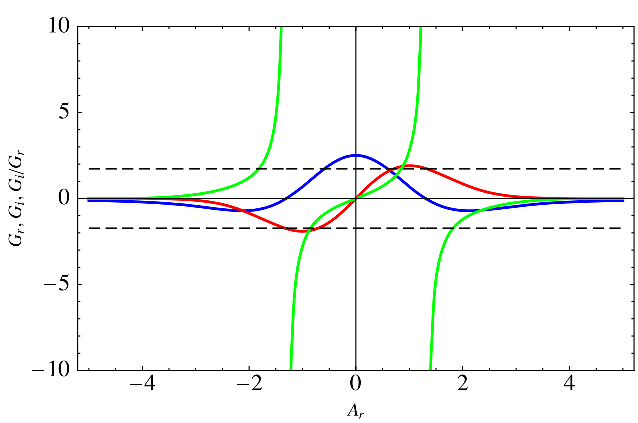

FIG. 13. The functions $G_r(A_r)$ (blue line), $G_i(A_r)$ (red line), and $G_i(A_r)/G_r(A_r)$ (green line) with real A_r and positive η. The horizontal dashed lines indicate $G_i/G_r = \pm\sqrt{3}$.

A. CSR instability threshold

The impedance model for free-space steady-state CSR is

$$Z_\parallel(k) = \frac{Z_0}{3^{1/3}}\left(\frac{\sqrt{3}}{2} + \frac{1}{2}i\right)\Gamma\left(\frac{2}{3}\right)(kR)^{1/3}, \tag{49}$$

where $\Gamma(z)$ is the Gamma function. Note that the real and imaginary parts have the same scaling law over k, resulting in $Z_r/Z_i = \sqrt{3}$. The threshold bunch current is further simplified as

$$f_{\mathrm{th}} = \frac{3}{4G_i Z_r}. \tag{50}$$

Applying $Z_r/Z_i = \sqrt{3}$ to Eq. (46) and solving the equation numerically, we find two solutions $A_{r1} \approx 0.85$ and $A_{r2} \approx 1.82$ (see the crossing points of the green lines and dashed black lines in the right half plane of Fig. 13), which, respectively, correspond to $G_{i1} \approx 1.86$ and $G_{i2} \approx -1.09$. The positive and negative values of G_i correspond to the positive and negative slip factors, respectively. Finally, we can explicitly write down the formula for CSR single-bunch instability threshold:

$$I_{\mathrm{th}}(\lambda) = \frac{3^{5/6}(2\pi)^{5/3}}{2\Gamma(\frac{2}{3})G_i}\frac{(E/e)\eta\sigma_p^2\sigma_z}{Z_0 R^{1/3}\lambda^{2/3}}, \tag{51}$$

with $\lambda = 2\pi/k$ the CSR wavelength. Note that the signs of η and G_i should be the same since the single-bunch instability threshold should be positive. It is also seen that the threshold current becomes lower at longer CSR wavelength. The above formula can be compared with the scaling law of Eq. (12) in Ref. [7]:

$$I_{\mathrm{th}}(\lambda) \approx \frac{4\pi^{7/6}}{\sqrt{2}}\frac{(E/e)|\eta|\sigma_p^2\sigma_z}{Z_0 R^{1/3}\lambda^{2/3}}, \tag{52}$$

for positive slip factor. One can see that with $G_i \approx 1.86$, Eqs. (51) and (52) are very close to each other except for a small difference in the constant scaling factors (10.75 vs 10.61). With a negative slip factor, the CSR instability threshold is larger than that of the positive slip factor by a factor of $1.86/1.09 = 1.74$. This is also consistent with the finding of Ref. [7].

B. CWR instability threshold

With the free-space CWR impedance [Eq. (6)], Z_r/Z_i is a function of wave number k. It is not trivial to find a k-independent solution of A_r in Eq. (46), as we did for free-space steady-state CSR. The dispersion relation [Eq. (40)] can only be solved numerically. But with some observations of the CWR impedance, we can still find a simplified formulation for CWR instability. Note that in the low-frequency limit, there is $k \ll k_c$. Therefore, we can fairly assume $\ln(k_c/k) \gg 1$ when $k_c/k \gg 1$. This suggests that $Z_r/Z_i \to 0$ when $k_c/k \gg 1$. Then, for positive η, from Eq. (46), we will have $G_r(A_r) \approx \sqrt{2\pi}$ and $G_i(A_r) \approx 0$ with $A_r \approx 0$, resulting in a threshold of

$$f_{\rm th} \approx \frac{1}{\sqrt{2\pi} Z_i}. \tag{53}$$

Explicitly, it is written as

$$I_{\rm th}(\lambda) \approx \frac{8\pi\sqrt{2\pi}(E/e)\eta\sigma_p^2\sigma_z}{LZ_0\theta_0^2 \ln\frac{2k_w\lambda}{\pi\theta_0^2}}, \tag{54}$$

where $\lambda = 2\pi/k$ is the CWR wavelength and L is the total length of the wigglers. On the other hand, for negative η, $Z_r/Z_i \to 0$ suggests a large A_r for the solution of Eq. (46) (see Fig. 13) and results in a large threshold current compared to the case of positive η.

C. Impact of chamber shielding

In the previous analyses, the MWI thresholds for free-space steady-state CSR and CWR are formulated as a function of radiation wavelength. The formulas are valid for a condition when $\sigma_z \gg \lambda$ and suggest that the MWI threshold decreases as the radiation wavelength increases. Since the chamber shielding strongly modifies the function $Z_\parallel(k)$ for CSR and CWR impedances, one can expect the scaling laws of the MWI threshold will also change. In this subsection, we briefly review the impact of chamber shielding.

For CSR, the parallel plates shield the low-frequency fields and increase the CSR MWI threshold [8]. Consider parallel-plates shielding, Eqs. (51) and (52) are only valid at wavelengths $\lambda < \lambda_c^{\rm CSR}$ with the cutoff wavelength given by [4]

$$\lambda_c^{\rm CSR} = 2\sqrt{\frac{b^3}{R}}. \tag{55}$$

On the other hand, the closed chamber creates resonance spectra in the CSR impedance and may decrease the MWI threshold [9]. This seemingly contradictory conclusion can be intuitively explained as follows: The upper- and lower-chamber walls shield the low-frequency radiation fields and reduce the perturbation to the beam. The side walls of the chamber reflect the radiation fields and amplify the perturbation to the beam [5]. This side-walls reflection is also interpreted as a synchronization of the waveguide modes with the beam motion.

Similar to CSR, the parallel plates set a cutoff wavelength on the CWR at

$$\lambda_c^{\rm CWR} = \frac{4\pi k_w}{k_w^2 + \pi^2/b^2}, \tag{56}$$

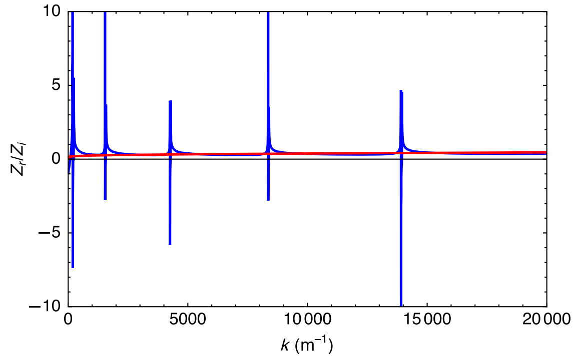

FIG. 14. Z_r/Z_i as a function of k for the DWs of the EIC backup ring cooler. The red line is for free-space steady-state CWR. The blue line is for parallel-plates steady-state CWR.

which can be found in Eq. (18) by taking $k_n = \pi/b$ for the lowest mode. When $b \ll \lambda_w = 2\pi/k_w$, Eq. (56) can be further simplified as

$$\lambda_c^{\rm CWR} \approx \frac{8b^2}{\lambda_w}. \tag{57}$$

Suppose $b \ll \lambda_w \ll R$ is applicable for damping rings, one can find that $\lambda_c^{\rm CWR} \gg \lambda_c^{\rm CSR}$ (it suggests $R \gg \lambda_w^2/(16b)$ is fairly satisfied). It implies that chamber shielding may be less effective in suppressing CWR than CSR in damping rings. In other words, to suppress CWR instability by chamber shielding, we may have to use a very small chamber height b. However, the resistive wall impedance, limitation on the dynamic aperture, and the length of the damping wiggler need to be addressed.

In addition to shielding, chambers synchronize the waveguide modes and the beam motion, generating narrow-band spikes in the CWR impedance. The narrow-band CWR impedances may decrease the instability threshold. Here we only give a qualitative discussion of the impact of chamber shielding on CWR instability. Using the same data as Fig. 2 for the case of the EIC backup ring cooler, we can plot Z_r/Z_i as shown in Fig. 14. We can see that Z_r/Z_i has large values on the resonance frequencies. According to Eq. (48), the CWR narrow-band impedance can reduce the CWR instability threshold.

V. CWR-DRIVEN MICROWAVE INSTABILITY IN THE EIC BACKUP RING COOLER

The storage ring cooler concept for the EIC project has been discussed in Ref. [15]. In this scheme, the emittance growth of the proton beam due to intrabeam scattering is counteracted by a cooling section in which the protons are copropagated with a high-brightness electron beam. To achieve the electron emittance required for cooling the proton beam, the electron ring needs significant radiation damping provided by 16 damping wigglers. Hence, the contribution of coherent wiggler radiation to the total

TABLE II. Main ring cooler parameters.

Energy, E_0	MeV	149.26
Circumference, C	m	426
Momentum compaction, α_c		-3.21×10^{-3}
Revolution period, T_0	μs	1.42
Energy loss, U_0	keV	5.933
Synchrotron tune, ν_s		0.0029
Damping time, σ_x, σ_τ	ms	31.7, 15.71
rf voltage, $V_{\rm rf}$	kV	19
rf frequency, $f_{\rm rf}$	MHz	98.5233
Harmonic number, h		140
Energy spread, σ_δ		6.5×10^{-4}
Bunch length, σ_s	mm	48

impedance of the ring can be significant. The challenges presented by collective effects are further compounded by the relatively low electron beam energy and high beam intensity. The main ring cooler parameters for the collective effects simulations and instability threshold estimation are presented in Table II.

A. Instability analysis

The CWR instability threshold can be found by numerically solving the dispersion relation Eq. (40) with free-space CWR impedance. The results can be compared with the prediction by Eq. (54). For demonstration, we choose $I = 2.5$ mA and scan λ to find $A(\lambda)$ satisfying Eq. (40), as shown in Fig. 15. It can be seen that for wavelengths $\lambda > 5.7$ mm, there is $\mathrm{Im}[\Omega] > 0$ and the beam will be unstable. Varying the bunch current and repeat solving the dispersion relation, we can determine the threshold bunch current as a function of CWR wavelength. At $\mathrm{Im}[A] = 0$, $\mathrm{Re}[A] < 1$ is guaranteed due to the property of free-space CWR impedance at low-frequency limit. Note that small $\mathrm{Re}[A]$ justifies Eq. (53).

For the case of EIC backup ring cooler, the bunch current threshold as a function of CWR wavelength is plotted in Fig. 16. One can see that the approximate formula agrees

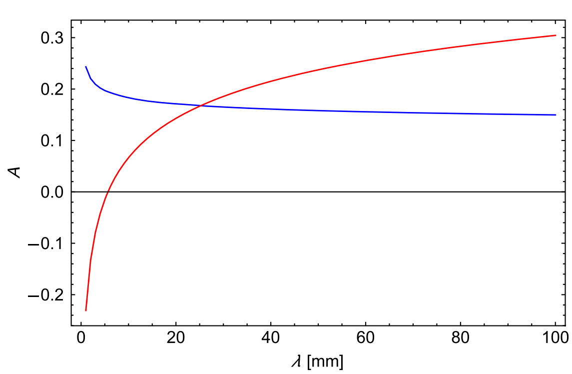

FIG. 15. Solution of dispersion relation with $I = 2.5$ mA for storage ring cooler. Blue and red lines indicate real and imaginary parts of A.

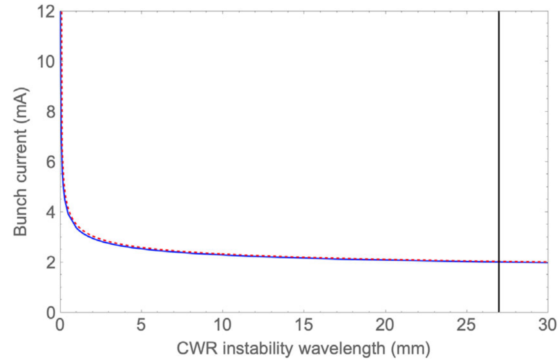

FIG. 16. Bunch current threshold as a function of CWR instability wavelength. Blue solid line is by solving Eq. (37). Red dashed line is by Eq. (54). The black solid line is the cutoff wavelength.

well with the direct solution of the dispersion relation. Equation (54) also indicates how one might increase the CWR-driven instability threshold: (i) increase the machine parameter $(E/e)\alpha_c\sigma_p^2\sigma_z$ and (ii) reduce the bending angle θ_0.

B. Vlasov-Fokker-Planck simulations

This section presents predictions obtained using Vlasov-Fokker-Planck simulations for the EIC ring cooler parameters presented in Table II and several impedance models of the damping wiggler. For this purpose, we wrote a Vlasov-Fokker-Planck code that splits the update into its conservative (Vlasov) and dissipative (Fokker-Planck) parts. The former Vlasov step is done using the method of Cheng and Knorr [23], wherein the distribution is transported along the particle trajectories and interpolated using cubic splines. The latter Fokker-Planck update is performed using the well-known Crank-Nicolson method. This basic algorithm was brought to accelerators in, e.g., [24]. Finally, we apply the collective force by taking a Fast Fourier transform of the current profile and using the impedance. The required resolution is obtained by using typically 512 spatial and momentum points over 5σs and padding the temporal current profile with zeroes to get sufficient frequency resolution for $Z_\parallel$.

The impedance models that we consider here include unshielded CWR, the parallel plate impedance [Eq. (11)], and that obtained for a rectangular chamber using CSRZ. In the latter case, the parabolic equation used by CSRZ gives unphysical results at very low frequencies, particularly, for $\mathrm{Im}Z_{||}$. Hence, we have reconstructed the low-frequency impedance by smoothly matching the numerical impedance obtained from CSRZ to that of the parallel plates model as $k \to 0$.

It turns out that these results will be easier to understand if we first consider the case where the cooler has positive momentum compaction, $\alpha_c > 0$, and Fig. 17 shows how the energy spread and bunch length depend upon the single

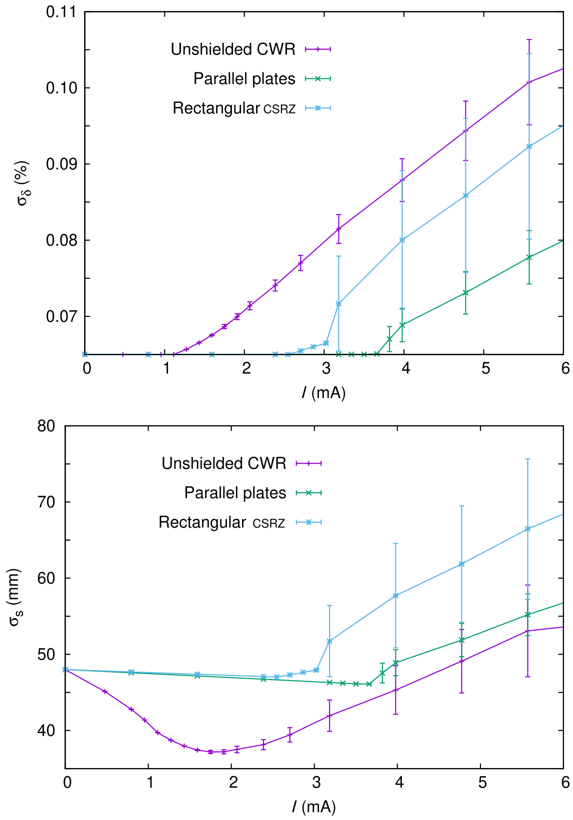

FIG. 17. Energy spread and bunch length dependence on the single bunch current for three different impedance models and $\alpha_c > 0$: the unshielded CWR (purple), the parallel plates model of Fig. 3 (green), and the predictions of CSRZ shown in Fig. 6 (blue). The ring is described in Table II but has positive $\alpha_c = 3.21 \times 10^{-3}$.

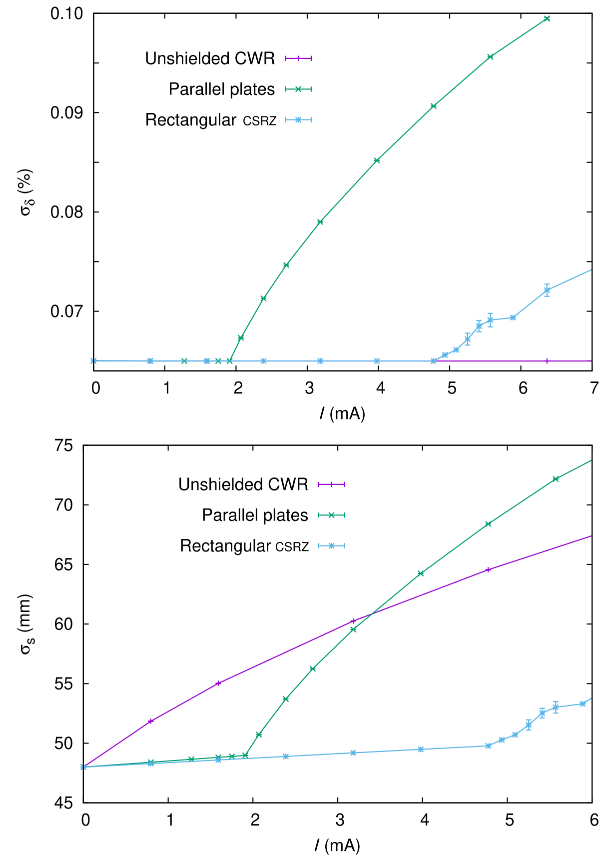

FIG. 18. Energy spread and bunch length dependence on the single-bunch current for three different impedance models and $\alpha_c < 0$: the unshielded CWR (purple), the parallel plates model of Fig. 3 (green), and the predictions of CSRZ shown in Fig. 6 (blue). The ring parameters are in Table II.

bunch current for $\alpha_c = 3.21 \times 10^{-3}$. The top plot predicts a microwave instability threshold for coherent wiggler radiation to be at about 1.1 mA, which is somewhat less than the theoretical prediction ∼2 mA shown in Fig. 16. The instability threshold for the rectangular chamber impedance derived from CSRZ is just below 3 mA, while that predicted by the parallel plates model is ∼3.8 mA. Hence, the two-chamber impedance models have instability thresholds that are within 25% of each other, being a factor of 2.5 to 3.5 times higher than that of the unshielded CWR.

The lower plot of Fig. 17, which shows the bunch length as a function of single-bunch current, helps explain some of the observed discrepancies in the microwave instability thresholds. In particular, the unshielded CWR leads to significantly more bunch shortening than the chamber impedance model since the chamber walls shield the low-frequency components of the impedance. The bunch shortening from CWR will in turn lead to a larger peak current for a given I, which in turn results in a lower microwave instability threshold. Nevertheless, the observed difference in peak current is only at the 25%–50% level and therefore does not completely explain the differences in $I_b^{\rm th}$.

When the momentum compaction is negative, $\alpha_c < 0$, the theoretical analysis predicted a larger microwave instability threshold for both the CSR and unshielded CWR impedance than the case when $\alpha_c > 0$. In addition, we expect that bunch lengthening may further increase $I_b^{\rm th}$. We plot the simulation predictions for the ring cooler with $\alpha_c < 0$ in Fig. 18. The top plot shows no evidence of the microwave instability for the unshielded CWR impedance when $I < 7$ mA, and in fact, we found no energy spread growth for currents $I < 15$ mA. However, the significant bunch lengthening shown in the bottom would make this case undesirable for the ring cooler. The prediction for the rectangular chamber using the CSRZ impedance indicates an instability threshold that is ≈1.7 times larger than the case when $\alpha_c > 0$. Interestingly, this is what is predicted by the CSR theory; while this relation may result from the similarity of short-range wakefields as was discussed previously, we do not think there is sufficient evidence for such a conclusion.

Furthermore, the collective behavior predicted for the parallel plate impedance mode is significantly different. Specifically, the microwave threshold current is lower than

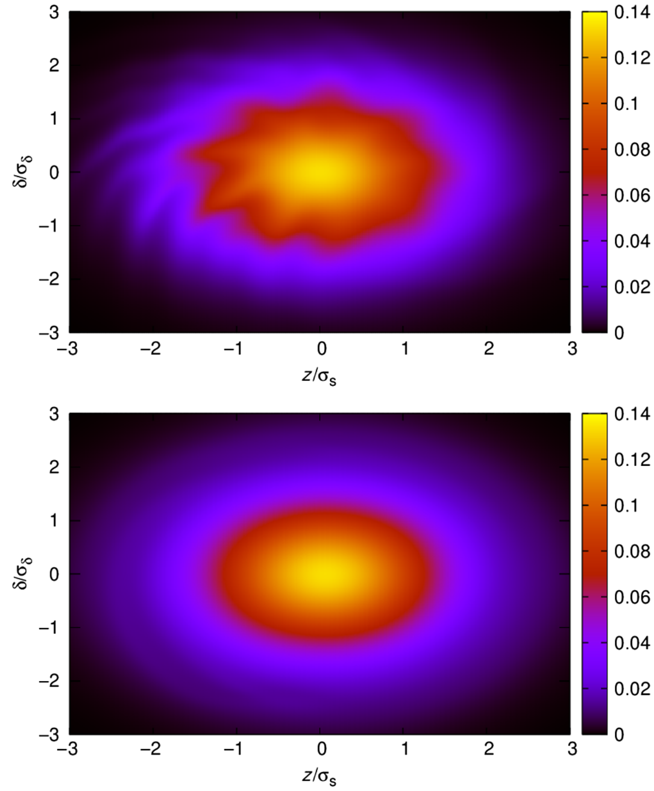

FIG. 19. Unstable phase space for $\alpha_c < 0$ and the rectangular chamber impedance from CSRZ at 5.6 mA (top) and the parallel plate impedance at 2.7 mA (bottom). The former shows evidence of the narrow-band impedance driving the instability, whereas the latter is characterized by a broadband halo.

that when $\alpha_c > 0$, and we observe significant bunch lengthening when $I > I_{\mathrm{th}}$. We believe that these differences are related to the following qualitative difference in the unstable motion. For all other cases considered, one can clearly identify a high-frequency signature in the instability. We show one such example in the top panel of Fig. 19, wherein we plot the phase space of the unstable beam for the rectangular CSRZ impedance and $\alpha_c < 0$ at $I = 5.6$ mA. Here, one can see how the impedance drives a high-frequency perturbation that gets carried by the synchrotron motion. Similar structures can be observed just above the threshold for all cases when $\alpha_c > 0$. This should be contrasted with the bottom panel of Fig. 19, which depicts the phase space of an unstable beam when $I = 2.7$ mA for the parallel plate impedance with $\alpha_c < 0$. In this case, there is no apparent structure, rather the bunch lengthening and energy spread growth are associated with the development of a diffuse halo of particles. We presently do not have a clear explanation for why this qualitative difference arises.

VI. SUMMARY

We studied the microwave instability in storage rings driven by CWR impedance in the wave number range of $1/\sigma_z \ll k \ll k_c$. The field dynamics and the difference between the three models for CWR impedance were discussed in detail. For parallel-plates shielding, we developed a simple formula of CWR impedance which is useful for cross-checking of the numerical results. There is no full analytic theory for rectangular-chamber shielding yet. Therefore, we use the CSRZ code to obtain the impedance data for analytical and numerical calculations.

We presented a simple method of solving the dispersion relation [Eq. (40)] to detect the MWI threshold driven by high-frequency impedances (i.e., impedances at $k \gg 1/\sigma_z$). The method was tested using the free-space steady-state CSR impedance. It successfully reproduces the CSR instability threshold found in Ref. [7] for both negative and positive slippage factors. For the free-space steady-state CWR impedance, the method predicts a simple scaling law of the MWI threshold for positive slippage factor and also shows that the MWI threshold can be very high for negative slippage factor. The analytical approach is used to explain the numerically simulated results using a VFP solver.

By considering three different models of CWR impedances and wakefields, free-space steady-state, parallel-plates shielding steady-state, and rectangular-chamber shielding model, we summarize that the short-range wakefield does not change dramatically, while the long-range wakefield depends strongly on the presence of the vacuum chamber. For the case of the EIC backup ring cooler, which has a large enough k_w, we found a 3.1-GHz frequency shift of the beam spectra simulated by the CSRZ code. The difference is due to the parabolic equation applied in the CSRZ code while the analytical approach is based on solving Maxwell's equations. The resonance modes of the CWR narrow-band impedance have been identified and classified.

The numerical Vlasov-Fokker-Planck simulations show that the instability threshold depends on the CWR impedance and especially on the low-frequency part of the longitudinal impedance and sign of the momentum compaction. The microwave instability threshold for $\alpha_c < 0$ gets higher for CWR impedance to be compared with the results for $\alpha_c > 0$, while in a case of the geometric impedance is vice versa. In a case of the EIC backup ring cooler and machine and DW parameters discussed in this paper, the estimated longitudinal microwave instability threshold due to the CWR impedance of 16 DWs is $I_{\mathrm{th}} = 5$ mA, which is smaller than 31 mA of Ref. [15] for slightly higher energy spread. Based on the recent progress in the optimization of the ring cooler parameters, the single-bunch current has been reduced up to ~10 mA. Further increasing the energy spread by a factor of 2 (up to 1.2×10^{-3}) can help to increase the microwave instability threshold up to ~20 mA [see Eq. (54)].

However, for a more accurate analysis of the longitudinal beam dynamics, the total longitudinal impedance budget, including the impedance of the vacuum system (geometric and resistive wall) and CSR impedance (dipole magnets), needs to be calculated (For example, see Ref. [27] for a case of SuperKEKB LER where the high-frequency CSR plays a marginal role.). The geometric and resistive-wall impedances cause potential-well distortion and consequently modify the longitudinal bunch profile as well as the synchrotron tune spread. This will affect the CWR effects on the microwave instability, as seen in the VFP simulations in Sec. V B. Since the vacuum system for the EIC backup ring cooler is not presently known, we can get a sense of the relative contribution of the vacuum components by scaling the NSLS-II total impedance, $Z/n = 0.4\ \Omega$ [25,26]. Scaling the NSLS-II circumference of 792 m and half-aperture of 12.5 mm to the 426-m circumference and a 30-mm Cu beam pipe radius of the cooler ring, we expect the cooler to have a $Z/n \approx 47\ \mathrm{m}\Omega$. This would imply a microwave instability threshold of $\approx$30 mA according to the Keil-Schenell-Boussard criterion [28], which is well above the observed $I_{\mathrm{th}} \sim 5$ mA due to 16 DWs found in this paper. This simple estimate also suggests that the CWR is the dominant source in determining the microwave instability threshold at the EIC backup ring cooler. The CSR impedance from the dipole magnets contributes to high-frequency impedance, which plays a role similar to the CWR impedance in determining the microwave instability threshold. In fact, the microwave instability in storage rings dominated by CSR impedances at high frequencies (i.e., $k \gg 1/\sigma_z$) has been intensively investigated in light sources (for example, see Refs. [9,21,29–31]).

Another way to get a feel for the contribution strength of 16 DWs is to compare the wakefields. In Fig. 20, we compare the total longitudinal wakefields simulated for the electron storage ring (ESR) of the EIC project vs 16 DWs for the EIC backup ring cooler with a 0.3-mm (1 ps) bunch length. The character of the two wakes is very different. The negative inductance of the 16 DWs (magenta line) is striking while the more resistive wakefield of the ESR (blue line) is typical of an optimized storage ring. The difference

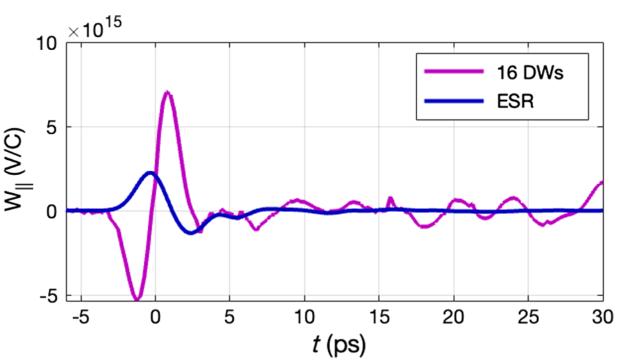

FIG. 20. Comparison of the total longitudinal wakefields for the Electron Storage Ring (ESR) of the EIC project vs 16 DWs for the backup ring cooler.

is particularly striking since the circumference of the ESR is 9 times the circumference of the cooler ring. Given the cooler ring energy of 150 MeV and ampere class beams, it is not surprising beam stability is a concern.

ACKNOWLEDGMENTS

This work was supported by Brookhaven Science Associates, LLC under Contract No. DE-SC0012704 with the U.S. Department of Energy. The work by R. Lindberg was supported by Department of Energy Contract No. DE-AC02-06CH11357. We would like to thank G. Stupakov for the fruitful discussion of some results.

[1] T. Agoh and K. Yokoya, Calculation of coherent synchrotron radiation using mesh, Phys. Rev. ST Accel. Beams **7**, 054403 (2004).

[2] D. Gillingham and T. Antonsen Jr, Calculation of coherent synchrotron radiation in toroidal waveguides by paraxial wave equation, Phys. Rev. ST Accel. Beams **10**, 054402 (2007).

[3] G. Stupakov and I. Kotelnikov, Calculation of coherent synchrotron radiation impedance using the mode expansion method, Phys. Rev. ST Accel. Beams **12**, 104401 (2009).

[4] T. Agoh, Steady fields of coherent synchrotron radiation in a rectangular pipe, Phys. Rev. ST Accel. Beams **12**, 094402 (2009).

[5] D. Zhou, K. Ohmi, K. Oide, L. Zang, and G. Stupakov, Calculation of coherent synchrotron radiation impedance for a beam moving in a curved trajectory, Jpn. J. Appl. Phys. **51**, 016401 (2011).

[6] G. Stupakov and D. Zhou, Analytical theory of coherent synchrotron radiation wakefield of short bunches shielded by conducting parallel plates, Phys. Rev. Accel. Beams **19**, 044402 (2016).

[7] G. Stupakov and S. Heifets, Beam instability and microbunching due to coherent synchrotron radiation, Phys. Rev. ST Accel. Beams **5**, 054402 (2002).

[8] K. L. Bane, Y. Cai, and G. Stupakov, Threshold studies of the microwave instability in electron storage rings, Phys. Rev. ST Accel. Beams **13**, 104402 (2010).

[9] Y. Cai, Scaling law of coherent synchrotron radiation in a rectangular chamber, Phys. Rev. ST Accel. Beams **17**, 020702 (2014).

[10] J. Wu, T. O. Raubenheimer, and G. V. Stupakov, Calculation of the coherent synchrotron radiation impedance from a wiggler, Phys. Rev. ST Accel. Beams **6**, 040701 (2003).

[11] G. Stupakov and D. Zhou, Longitudinal impedance due to coherent undulator radiation in a rectangular waveguide, SLAC Report No. SLAC-PUB-14332, 2010.

[12] J. Wu, G. Stupakov, T. Raubenheimer, and Z. Huang, Impact of the wiggler coherent synchrotron radiation impedance on the beam instability and damping ring optimization, Phys. Rev. ST Accel. Beams **6**, 104404 (2003).

[13] A. Wolski and W. Decking, Damping ring designs and issues, in *Proceedings of the 2003 Particle Accelerator Conference, Portland, OR* (IEEE, New York, 2003), Vol. 1, pp. 652–656.
[14] F. Zimmermann, M. Korostelev, D. Schulte, T. Agoh, and K. Yokoya, Collective effects in the CLIC damping rings, in *Proceedings of the 21st Particle Accelerator Conference, Knoxville, TN, 2005* (IEEE, New York, 2005), pp. 1312–1314.
[15] H. Zhao, J. Kewisch, M. Blaskiewicz, and A. Fedotov, Ring-based electron cooler for high energy beam cooling, Phys. Rev. Accel. Beams **24**, 043501 (2021).
[16] F. Willeke *et al.*, Electron Ion Collider Conceptual Design Report, EIC CDR Brookhaven National Laboratory, 2021.
[17] D. Zhou, Coherent synchrotron radiation and microwave instability in Electron Storage Rings, Ph.D. thesis, The Graduate University for Advanced Studies, 2011.
[18] Y. H. Chin, Coherent radiation in an undulator, Lawrence Berkeley Laboratory, CA, Technical Report No. LBL-29981, 1990.
[19] T. Agoh, Dynamics of coherent synchrotron radiation by paraxial approximation, Ph.D. thesis, University of Tokyo, 2004.
[20] H. Deruyter, Z. Farkas, H. Hoag, K. Ko, N. Kroll, G. Loew, R. Miller, R. Palmer, J. Paterson, K. Thompson *et al.*, Damped and detuned accelerator structures, Stanford Linear Accelerator Center, Menlo Park, CA, Technical Report No. SLAC-PUB-5322, 1990.
[21] Venturini, Marco, Robert Warnock, Ronald Ruth, and James A. Ellison, Coherent synchrotron radiation and bunch stability in a compact storage ring, Phys. Rev. ST Accel. Beams **8**, 014202 (2005).
[22] M. Korostelev, A. Wolski, and A. Thorley, Wake field analysis and modelling of microwave instability in the ILC damping ring, Nucl. Instrum. Methods Phys. Res., Sect. A **659**, 36 (2011).
[23] C. Z. Cheng and G. Knorr, The integration of the Vlasov equation in configuration space, J. Comput. Phys. **22**, 330 (1976).
[24] R. Warnock, K. Bane, and J. Ellison, Simulation of bunch lengthening and sawtooth mode in the SLAC damping rings, in *Proceedings of the European Particle Accelerator Conference, Vienna, 2000* (EPS, Geneva, 2000).
[25] A. Blednykh, G. Bassi, C. Hetzel, B. Kosciuk, V, and Smaluk, NSLS-II longitudinal impedance budget, Nucl. Instrum. Methods Phys. Res., Sect. A **1005**, 165349 (2021).
[26] A. Blednykh, G. Bassi, V. Smaluk, and R. Lindberg, Impedance modeling and its application to the analysis of the collective effects, Phys. Rev. Accel. Beams **24**, 104801 (2021).
[27] T. Abe, T. Ishibashi, Y. Morita, K. Ohmi, K. Shibata, Y. Suetsugu, M. Tobiyama, and D. Zhou, Impedance calculation and simulation of microwave instability for the main rings of SuperKEKB, in *Proceedings of the 5th International Particle Accelerator Conference, IPAC-2014, Dresden, Germany* (JACoW, Geneva, Switzerland, 2014), pp. 600–1602.
[28] D. Boussard, Observation of microwave longitudinal instabilities in the CPS, CERN Report No. LabII-RF-INT-75-2, 1975.
[29] J. Byrd, W. P. Leemans, A. Loftsdottir, B. Marcelis, Michael C. Martin, W. R. McKinney, F. Sannibale, T. Scarvie, and C. Steier, Observation of Broadband Self-Amplified Spontaneous Coherent Terahertz Synchrotron Radiation in a Storage Ring, Phys. Rev. Lett. **89**, 224801 (2002).
[30] E. Roussel, C. Evain, C. Szwaj, S. Bielawski, J. Raasch, P. Thoma, A. Scheuring *et al.*, Microbunching Instability in Relativistic Electron Bunches: Direct Observations of the Microstructures Using Ultrafast YBCO Detectors, Phys. Rev. Lett. **113**, 094801 (2014).
[31] M. Brosi, J. L. Steinmann, E. Blomley, T. Boltz, E. Bründermann, J. Gethmann, B. Kehrer *et al.*, Systematic studies of the microbunching instability at very low bunch charges, Phys. Rev. Accel. Beams **22**, 020701 (2019).